Andreas

Continental Shelf Research, Vol. 12, No. 4, pp. 471–498, 1992.
Printed in Great Britain.

0278–4343/92 $5.00 + 0.00

Astronomical and nonlinear tidal currents in a coupled estuary shelf system

ANDREAS MÜNCHOW,* ANN K. MASSE*† and RICHARD W. GARVINE*

(*Received* 26 *December* 1990; *accepted* 20 *May* 1991)

Abstract—We analysed the tidal content of current time series from 53 current meters at 31 mooring locations on the inner continental shelf in the vicinity of Delaware Bay, U.S.A. We distinguish between an astronomically forced short period flow field at diurnal and semi-diurnal frequencies and a nonlinearly generated long period tidal flow field. The latter operates at the difference frequencies of the former. We found short period tidal currents to vary from 90 cm s^{-1} at the mouth of the estuary to 8 cm s^{-1} only 30 km to the north. Tidal volume flux through the mouth generates intensified tidal currents on the shelf as far as 50 km away to the southeast.

At periods longer than 2 weeks we detected tidal currents with amplitudes from 1 to 3 cm s^{-1} and phases indicative of a horizontally coherent flow field. We also estimated mean rectified tidal flow fields of about 2–7 cm s^{-1}. These thus contribute substantially to the overall mean currents on the shelf.

1. INTRODUCTION

TAYLOR (1920) predicted with an analytical model the horizontal distribution of tidal currents and sea level in shallow waters such as the Irish Sea. His predictions agreed qualitatively with observed tidal sea level variations along the Irish, Welsh and English coasts. The systematic field study of tidal currents in the coastal ocean, however, began only with modern mooring installations. HOWARTH and PUGH (1983) review observational techniques, analyses and results.

In this study we describe observations of the horizontal distribution of tidal currents on the inner continental shelf adjacent to a major estuary. We concentrate on astronomically forced short period (~12 h) and nonlinearly forced long period (>2 weeks) tidal flows. We also show how a major estuary influences the tidal circulation on the shelf.

Short period tidal current variations propagate along coasts as astronomically forced Kelvin waves (BOWDEN, 1983). Such flows are readily observed and form the basis of tidal current atlases available for many coastal areas (MOODY *et al.*, 1984; U.S NAVAL OCEANOGRAPHIC OFFICE, 1965). The nonlinear terms in the equations of motion at diurnal and semi-diurnal frequencies generate rectified currents at the sum and difference frequencies of any two short period tides (IANNIELLO, 1977; TEE, 1980). In the following we will call tides at the difference frequencies long period tides, since their periods are

*College of Marine Studies, University of Delaware, Newark, DE 19716, U.S.A.
†Present address: E. I. duPont de Nemours and Co., Inc., P.O. Box 787, Niagara Falls, NY 14372, U.S.A.

generally larger than 2 weeks. A non-oscillatory or mean tidal flow field is also generated by each short period tide through nonlinearities. This steady flow field has been the focus of many modelling studies (IANNIELLO, 1977; TEE, 1980; WRIGHT and LODER, 1985; ZIMMERMAN, 1980). ZIMMERMAN (1976, 1981 and 1986) first addressed the mixing capabilities of rectified long period tides.

Still another interaction process is the coupling between the inner continental shelf and an estuary. Large estuaries such as Delaware Bay (U.S.A) or the Elbe (Germany) exchange huge volumes of water with the shelf at semi-diurnal periods. Intensified tidal currents on the shelf provide this volume and drive stronger long period tidal currents that affect the net import and export of matter from the estuary. Thus, estuary and shelf are a coupled tidal system.

Long period tidal signals are hard to detect in noisy records. WUNSCH (1967) and AUBREY and SPEER (1985) employed spectral analysis in order to extract signals at the frequency of the long period tides. The records had to be excessively long in order to resolve spectral lines with statistical significance. Wunsch needed 4 year-long sea level time series to describe the global response to long period astronomical forcing in the Pacific Ocean. BUTMAN *et al.* (1983), SMITH (1983) and MAGNELL *et al.* (1980) employed complex demodulation of velocity time series along with time and frequency domain correlation techniques to detect locally generated long period tidal currents on Georges Bank, U.S.A. and Canada. Finally, THOMPSON and WILSON (1987) used least squares techniques (DRONKERS 1964) to predict monthly and fortnightly flows near the Queen Charlotte Islands, British Columbia. The main obstacle all these studies encountered was noise which masked the tidal signal. Wind, buoyancy forcing and vorticity waves operate at similar frequencies and thus constitute noise in which the tidal signal is embedded. All the above studies tried to obtain statistically significant results by using very long time series, but these are not always available.

We compiled and analysed all available current data from an area 60 km to the north, south and east of the mouth of Delaware Bay, U.S.A. We used local wind and freshwater discharge data to reduce the noise from modestly long current meter records by removing the part of the current record that was coherent with these variables. The incoherent part of the currents we then subjected to a least squares analysis where we allow for gaps in our time series. In order to judge the reliability of the results from the harmonic analyses we needed an accurate error estimation technique. In Appendix A we compare different methods and describe the one we adopted. Section 2 lists pertinent details of the data set and its analysis; Section 3 discusses the dominant short period tidal flow field. There we also estimate volume fluxes and the vertical mixing power of these tidal currents. Sections 4 and 5 focus on the oscillatory long period tides and the mean rectified tidal flow field, respectively. We thus progress from high to low frequency tidal flow fields. Section 6 concludes the paper.

2. DATA SOURCES AND ANALYSIS

We examined current meter data collected by several institutions between 1983 and 1989 on the inner continental shelf within 60 km of the mouth of Delaware Bay (Fig. 1). Of the total of 31 mooring locations the University of Delaware maintained 16, while the National Ocean Service of the U.S. Department of Commerce and the U.S. Naval Oceanographic Office installed 10 and 5 moorings, respectively. Figure 2 shows all

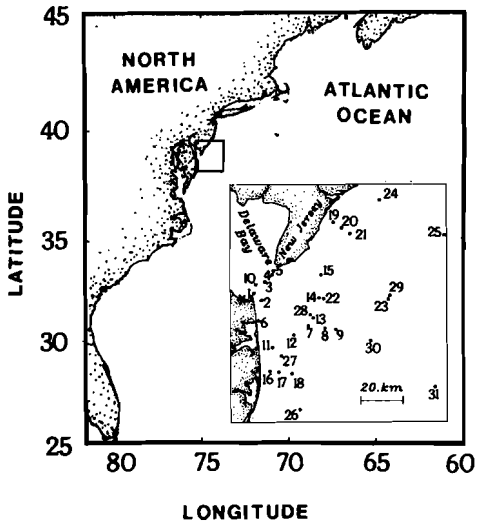

Fig. 1. Map of the study area. The insert is an enlargement of the rectangle at 39°N latitude and 75°W longitude. Mooring locations are shown as stars with numbers. The large star on land near mooring 1 indicates the coastal sea level stations at Lewes, Delaware.

mooring locations as vertical lines on a perspective view of the local bottom topography looking from the ocean landward. Most of the moorings, all of taut wire type with subsurface floatation, were located in the vicinity of the deep channel between the estuary mouth and the shelf.

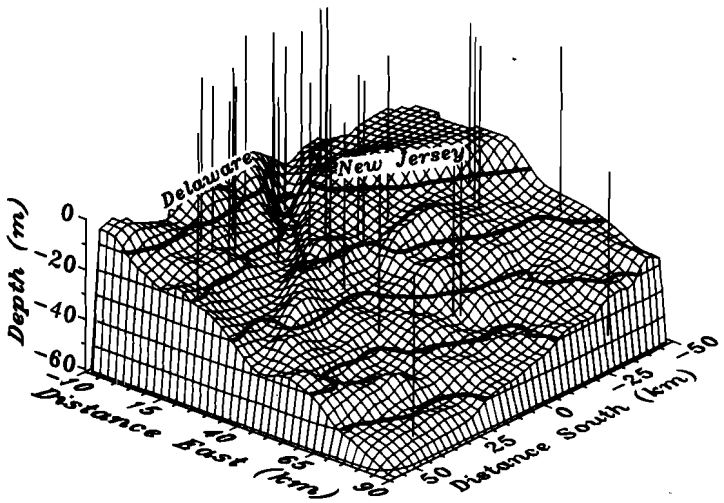

Fig. 2. Isometric projection of the bottom topography for the inner shelf off Delaware Bay. The view is from above and toward the northwest. The mouth of Delaware Bay appears as the valley separating the Delaware and New Jersey coasts. Isobaths are at 10 m intervals. Vertical lines simulate mooring wires for the current meters that provided the data; the lowest point on each line marks the location of the mooring anchor on the bottom. Note the deep channel that connects the Bay mouth with the inner shelf.

In Table 1 we list pertinent details of the current data collection. Water depth at the mooring sites ranged from 8 to 52 m. Between one and three instruments were attached to each mooring wire at depths ranging from 3 to 51 m. Record lengths, as measured in data days, varied widely as Table 1 shows. The shortest record contained 14 days of data, sufficient only to estimate the principal diurnal and semi-diurnal tidal constituents reliably, while the longest record consisted of 441 data days (mooring 14).

The duration of many of the records exceeded the amount of data days given in Table 1 because of gaps in the records during periods of instrument failure or mooring service. Since tidal currents originate from astronomical forces describable by a discrete set of harmonic constituents of known frequencies, we assume that the barotrophic tidal current response and parameters such as mean water depth and bottom friction are stationary in time. Therefore, we treat the tidal current properties as independent of time for each harmonic constituent.

Errors of estimated amplitudes and phases of each harmonic constituent arise from a variety of sources. Besides instrument error, which we neglect here, errors arise from the presence of motion produced by agents other than those of astronomical origin. Wind stress, density gradients, baroclinic (or internal) tides, coastally trapped waves, etc., all force currents that constitute a noisy background in which the tidal current signal is embedded. This is especially true for low frequency constituents which are often of small amplitude, difficult to detect, and reported only infrequently. Therefore, we provide uncertainty estimates for the amplitude and phase of each harmonic constituent. We tested different methods (FILLOUX and SNYDER, 1979; HELSTROM, 1960) which we discuss in Appendix A.

Commonly, least squares harmonic analysis applies to a single, equally spaced, discrete time series only (DRONKERS, 1964). We extended the formalism of Dronkers in order to apply it to any number of equally spaced time series, i.e. to time series that include gaps with missing data. We introduce a common time base for all series rather than an individual time base for each series. Harmonic analysis seeks to fit the following model to these data

$$u_i(t) = A_{i0} + \sum_{k=1}^{M} [A_{ik} \cos(\omega_k t) + B_{ik} \sin(\omega_k t)], \qquad i = 1,2. \tag{1}$$

A_{i0}, A_{ik}, and B_{ik} are coefficients to be found, t is the time, and the ω_k are known frequencies representing a tidal constituent. The subscript "i" denotes a horizontal velocity component. Subjecting this model to the least squares error constraint (DRONKERS, 1964) gives a system of $2M+1$ linear equations for each velocity component, represented by

$$\mathbf{F}\vec{x}_i = \vec{D}_i, \qquad i = 1,2 \tag{2}$$

where $\mathbf{F}$ is a symmetric $(2M + 1) \times (2M + 1)$ matrix depending upon the ω_k only, $\vec{x}_i$ is a vector containing the unknowns A_{i0}, A_{ik}, B_{ik}, and $\vec{D}_i$ is a data vector containing observations of u_i. We always analysed the short period constituents M_2, N_2, S_2, K_1, O_1 and M_4, while for records exceeding 45 days in length we analysed the long period tides M_m and M_{sf} as well. Thus, we generally chose $M = 6$ for short and $M = 8$ for long records. The only difference between DRONKERS (1964) and our harmonic analysis is the structure of the

Table 1. Details of current meter data sources

Mooring	North latitude	West longitude	Water depth (m)	Instrument depth (m)	Record length (days)	Instrument*
1	38°48.8′	75°04.9′	23	4	29	G
				21	47	G
2	38°46.9′	75°02.6′	18	4	153	G
				12	203	G
				17	141	G
3	38°51.6′	75°01.5′	12	6	48	G
				8	53	G
4	38°53.4′	74°59.1′	8	5	110	G
5	38°54.4′	74°58.7′	9	5	119	G
				8	103	G
6	38°41.8′	75°03.6′	10	5	106	E174
7	38°40.5′	74°47.6′	20	5	45	E174
				15	45	E105
8	38°39.9′	74°42.3′	20	5	61	E174
				15	61	E105
9	38°39.6′	74°38.8′	30	5	93	S4
				25	67	S4
10	38°50.9′	75°04.4′	44	20	361	S4
11	38°35.1′	74°59.2′	14	11	144	S4
12	38°38.2′	74°52.2′	25	3	225	S4
				16	285	S4
13	38°42.5′	74°46.0′	19	16	333	S4
14	38°47.5′	74°44.2′	15	6	424	S4
				12	441	S4
15	38°53.2′	74°43.6′	17	14	33	S4
16	38°29.2′	75°00.0′	14	6	95	S4
				10	50	S4
17	38°29.0′	74°57.2′	17	6	95	S4
				10	50	S4
18	38°28.6′	74°53.0′	18	6	91	S4
19	39°06.4′	74°39.4′	14	6	99	S4
				10	99	S4
20	39°05.0′	74°36.7′	13	6	54	S4
				10	45	S4
21	39°03.6′	74°34.1′	15	6	54	S4
22	38°47.3′	74°42.7′	18	8	14	G
				11	15	G
				15	30	G
23	38°47.1′	74°22.1′	35	8	15	G
				20	15	G
				32	14	G
24	39°12.0′	74°24.8′	18	7	229	G
				10	156	G
				15	156	G
25	39°03.1′	74°04.3′	31	8	84	G
				15	108	G
				27	154	G
26	38°19.6′	74°50.4′	18	15	29	G
27	38°33.0′	74°56.4′	15	14	24	E174
28	38°43.3′	74°47.0′	15	14	24	E174
29	38°48.1′	74°21.5′	36	35	24	E174
30	38°36.7′	74°27.7′	35	34	24	E174
31	38°25.2′	74°07.4′	52	51	24	E174

*G: Grundy 9021G; E174: Endeco 174; E105: Endeco 105; S4: InterOcean S4.

matrix **F**. Dronkers references the data relative to the time center of the period of measurements; many elements of **F** are then zero. We used a common time reference for all series, instead. Few matrix elements are then zero, but with present computers matrix inversion is nevertheless practical. FOREMAN (personal communication) developed a similar harmonic analysis program. In the following we present all results from the harmonic analysis as ellipse parameters, explained below, which we compute from $\vec{x}_i$ according to MOOERS (1973).

3. M_2 TIDAL CURRENTS

In Table 2 we show results of our harmonic analysis for eight constituents from one of our longest current data records, that of mooring 14 (see Fig. 1 for location) at depth 6 m with water depth 15 m where we had 424 data days. The constituents appear in the order of their major axis amplitudes. The angles of the major axes are in degrees measured positively counterclockwise from east. We give the major axis amplitudes together with their estimated uncertainty. The ratio of the minor to major axis amplitude we define as ε, the ellipticity of the ellipse traced by the tidal current hodograph. The direction of current vector rotation is counterclockwise for ε positive, clockwise for ε negative. The current phase indicates the phase lead of maximum current relative to predicted M_2 high water at the coast nearby at Lewes, Delaware (Fig. 1). The relation of phase to the current vector we describe in Appendix B. Table 2 also shows the uncertainty of the phase, even though these uncertainties are overestimated (see Appendix A). The property SNR denotes the signal to noise ratio that we obtained for the major axis component from spectral analysis for use in calculating the uncertainty estimates, as described in Appendix A.

The constituents listed divide naturally into four classes by period: the quarter-diurnal M_4 constituent, the semi-diurnal constituents, M_2, N_2, and S_2, the diurnal constituents, O_1 and K_1, and the long period constituents, M_{sf} and M_m.

The M_2 constituent is dominant in amplitude and contains about 90% of the tidal current kinetic energy. This dominance we found in all the other current records. Consequently, we will limit our discussion of the short period (less than about 1 day) tidal currents to M_2 alone. In Section 4 we present results for the M_{sf} and M_m constituents. The associated steady state flows we discuss in Section 5.

Table 2. *Tidal current constituents at mooring* 14, *water depth* 15 m, *and instrument depth* 6 m

Constituent	Period (days)	Major axis angle (°)	Major axis amplitude (cm s^{-1})	ε	Phase (°)	SNR
M_2	0.518	152	25.1 ± 0.0	−0.08	92 ± 2	2267
N_2	0.527	154	4.9 ± 0.0	−0.09	15 ± 3	1118
S_2	0.500	151	4.4 ± 0.0	−0.04	19 ± 6	306
O_1	1.076	191	2.5 ± 0.2	0.07	108 ± 22	26
K_1	0.997	129	2.3 ± 0.1	0.38	87 ± 19	33
M_m	27.555	114	0.6 ± 0.5	−0.63	95 ± 73	2
M_4	0.259	123	0.5 ± 0.1	0.19	−32 ± 36	10
M_{sf}	14.765	102	0.2 ± 0.6	−0.91	−59 ± 140	1

In Table 3 we list the M_2 tidal properties for all the current meter records, as well as for the M_2 tidal height at Lewes, Delaware (see Fig. 1). For the great majority of the records the uncertainties in amplitude are quite small because of the large values of SNR. The results for moorings with more than one current meter, for example, moorings 12, 14 and 24, show that M_2 properties generally varied little in the vertical. Major axis directions were nearly the same, while toward the bottom, currents were usually somewhat slower, phase leads somewhat greater, and ellipticities less negative. These are all well known properties of barotropic tidal currents subject to bottom friction (MAAS and VAN HAREN, 1987). Consequently, with the exception of the following account for the mouth of Delaware Bay, we will limit our discussion of the M_2 currents to the horizontal variation of properties rather than the vertical.

Figure 3 shows amplitudes and phases for M_2 current over a vertical section (see Fig. 5) across the mouth of the Bay. The view is into Delaware Bay with the Delaware coast on the left. The data sources were the records from moorings 1, 3, 4, and 5 (see Fig. 1 for locations); the corresponding current meter locations are noted on the figure from left to right. The current amplitude is for the component roughly normal to the section. Note the deep channel near the Delaware coast shown in the lower panel.

The bulk of the M_2 tidal volume flux passes through this channel which has a typical depth of over 20 m and width of about 6 km. As we discuss further below, the continuation of this channel seaward toward the south-southeast forms the centerline for the intensified currents we found on the inner shelf. Over the Bay mouth section the M_2 current amplitude is about 70 cm s^{-1}. Such current amplitudes are typical inside the estuary (NATIONAL OCEAN SERVICE, 1986) but are much greater than those on the Middle Atlantic Bight shelf away from large estuaries (MAYER, 1982). The current amplitude varies over the section between about 50 and 90 cm s^{-1} with larger amplitudes occurring near the surface where the channel is deep. As Table 3 shows, the major axis directions for the records on this section (moorings 1, 3, 4, and 5) are all close to 135°, i.e. toward northwest and nearly normal to the section. The currents are nearly rectilinear with $|\varepsilon| \leq 0.06$. The current phase varies between 60 and 80°, indicating that at the time of high water the current is still landward (flood phase). The phase is larger nearer the bottom and in shallower water on the right, so that the "tide turns" earlier there.

By interpolating and integrating these amplitude and phase values for the M_2 current across this vertical section at the mouth we computed the tidal transport V_t and the Stokes mean transport $\bar{V}_s$. We define V_t in the harmonic form

$$V_t = \gamma \cos(\omega_{M_2} t + \Phi) \tag{3}$$

where ω_{M_2} is the M_2 angular frequency and t is relative to the time for M_2 high water at Lewis; γ is the transport amplitude; and Φ its phase. We found

$$\gamma = (1.47 \pm 0.05) x 10^5 \text{ m}^3 \text{ s}^{-1}$$
$$\Phi = 69° \pm 4°$$

where the uncertainties given are based on the error analysis results of Table 3. Because the mean cross-sectional area at the mouth is 2.58×10^5 m^2, the sectionally-averaged M_2 current amplitude is then 57.0 cm s^{-1}.

We computed the mean Stokes transport following the form of LONGUET-HIGGINS (1969) for a channel. This gives the local Stokes transport per unit breadth as

Table 3. M_2 *tidal properties*

Mooring	Water depth (m)	Instrument depth (m)	Major axis angle (°)	Major axis amplitude (cm s^{-1})	ε	Phase (°)	SNR
Lewes sea level	—	—	—	9.1 cm	—	0	—
Model*	24	—	150	13.2	−0.54	90	—
1	23	4	127	94.3 ± 0.3	−0.03	56 ± 4	652
		21	129	41.7 ± 0.3	0.03	90 ± 6	369
2	18	4	123	80.2 ± 0.1	−0.09	45 ± 4	1048
		12	124	61.0 ± 0.2	0.11	57 ± 4	749
		17	127	34.9 ± 0.2	0.22	60 ± 6	356
3	12	6	126	60.8 ± 0.2	0.02	72 ± 5	525
		8	131	43.1 ± 0.1	0.03	71 ± 5	584
4	8	5	139	43.5 ± 0.1	0.04	89 ± 4	728
5	9	5	137	69.6 ± 0.1	0.04	88 ± 2	2120
		8	135	51.0 ± 0.0	0.06	90 ± 2	4326
6	10	5	120	24.1 ± 0.4	−0.01	79 ± 10	127
7	20	5	148	21.0 ± 0.1	−0.18	55 ± 6	392
		15	132	15.2 ± 0.3	0.05	80 ± 11	114
8	20	5	160	18.7 ± 0.3	−0.32	76 ± 11	107
		15	135	26.7 ± 0.3	−0.08	87 ± 9	172
9	30	5	160	16.5 ± 0.2	−0.20	79 ± 9	146
		25	141	12.3 ± 0.2	−0.03	121 ± 9	146
10	44	20	120	60.1 ± 0.3	0.02	61 ± 6	387
→ 11	~~14~~	~~6~~ 11	106	17.6 ± 0.2	0.00	86 ± 9	344
12	22	3	129	24.2 ± 0.2	−0.16	52 ± 8	206
		18	117	22.2 ± 0.2	−0.04	74 ± 8	238
13	19	15	139	15.9 ± 0.1	0.05	102 ± 5	613
14	15	6	152	25.1 ± 0.0	−0.08	92 ± 2	2267
		12	150	22.1 ± 0.0	−0.02	102 ± 3	1228
15	17	13	159	16.8 ± 0.2	0.21	131 ± 8	212
16	14	6	97	17.2 ± 0.3	−0.20	72 ± 11	99
		10	86	16.3 ± 0.4	−0.16	89 ± 13	80
17	17	6	97	16.8 ± 0.4	−0.28	55 ± 12	85
		10	88	18.3 ± 0.5	−0.36	61 ± 13	73
18	18	6	111	19.9 ± 0.3	−0.34	61 ± 10	124
19	14	6	202	7.1 ± 0.3	−0.02	92 ± 16	52
		10	199	6.5 ± 0.3	0.16	108 ± 17	42
20	13	6	187	8.2 ± 0.4	−0.10	121 ± 17	39
		10	182	7.4 ± 0.3	0.07	114 ± 16	46
21	15	6	179	10.8 ± 0.4	−0.16	115 ± 15	52
22	18	8	150	21.6 ± 0.2	−0.12	81 ± 8	215
		11	151	21.5 ± 0.2	−0.02	91 ± 8	183
		15	147	16.1 ± 0.3	0.04	96 ± 11	99
23	35	8	153	13.6 ± 0.6	−0.36	91 ± 16	47
		20	144	9.6 ± 0.3	−0.32	105 ± 14	61
		32	140	8.3 ± 0.2	−0.10	119 ± 14	67
24	18	7	157	7.7 ± 0.2	−0.37	113 ± 12	92
		10	153	7.3 ± 0.0	−0.31	124 ± 1	8877
		15	149	5.5 ± 0.1	−0.17	130 ± 10	117

wrong 5/17/2007

Continued

Table 3. Continued

Mooring	Water depth (m)	Instrument depth (m)	Major axis angle (°)	Major axis amplitude (cm s^{-1})	ε	Phase (°)	SNR
25	31	8	144	9.4 ± 0.3	−0.41	125 ± 13	72
		15	144	11.1 ± 0.0	−0.45	120 ± 5	538
		27	123	8.4 ± 0.1	−0.29	131 ± 8	191
26	18	15	108	10.2 ± 0.6	−0.39	83 ± 19	35
27	15	14	117	21.5 ± 0.7	−0.03	93 ± 14	80
28	15	14	156	23.1 ± 0.2	0.23	88 ± 7	263
29	36	35	131	8.4 ± 0.1	−0.10	133 ± 10	136
30	35	34	134	14.0 ± 0.3	−0.28	102 ± 13	80
31	52	51	146	15.2 ± 0.4	−0.46	104 ± 13	72

*Model results are from BATTISTI and CLARKE (1982).

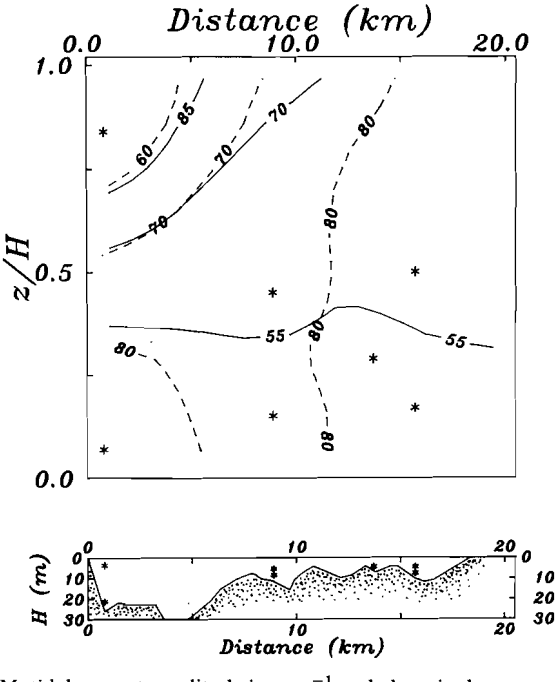

Fig. 3. Values of M_2 tidal current amplitude in cm s^{-1} and phase in degrees on a transect across the mouth of Delaware Bay (heavy line in Fig. 5). View is into the Bay with the Delaware coast on the left. "Star" symbols mark the locations of the current meters used at moorings 1, 3, 4 and 5 from left to right (see Fig. 1 and Tables 1 and 3). In the upper panel we show current amplitude and phase contours as solid and dashed lines, respectively. Here the ordinate is z/H where H is the local water depth and z is measured upward from the bottom. In the lower panel we show the distribution of H with distance.

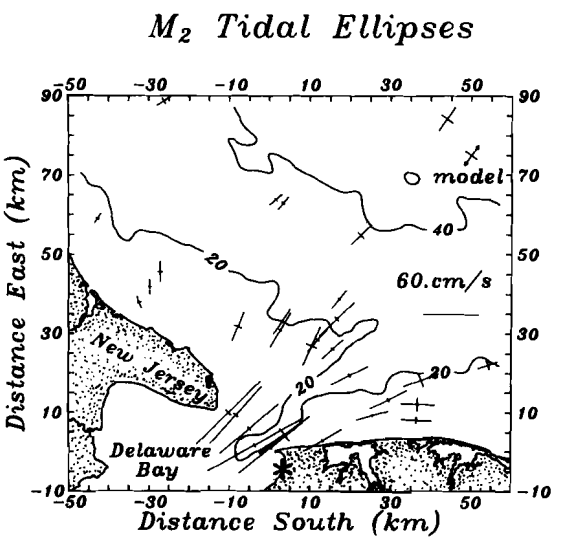

Fig. 4. Map of the principal axes for the M_2 tidal current for the deepest current meter record from each mooring. East is to the top. The speed scale appears at the center right. The axes denoted by "model" are from the results of BATTISTI and CLARKE (1982).

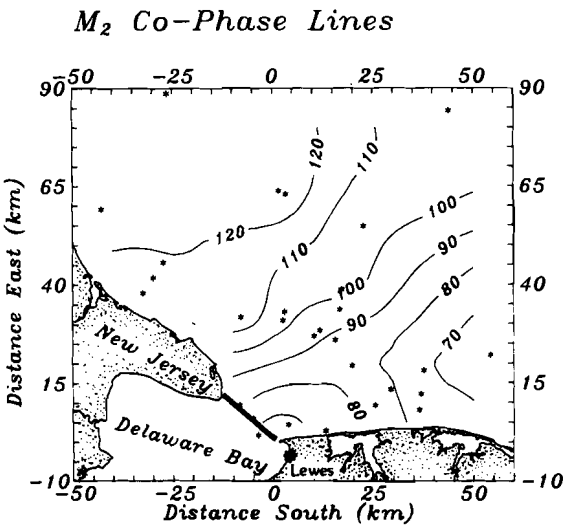

Fig. 5. Contour map of M_2 current phase. Phase is in degrees and relative to M_2 high water at the coast at Lewes, Delaware. Positive values indicate current leads sea level. See Appendix B for details of phase definition. Data were smoothed and contoured from the record of the deepest current meter at each mooring. "Star" symbols mark the mooring locations. The heavy line across the Bay mouth marks the section shown in Fig. 3.

$$\frac{d\bar{V}_s}{dy} = \frac{1}{2} a(y)b(y) \cos[\phi(y)] \tag{4}$$

where a is the M_2 surface current amplitude at across-channel location y; b is the M_2 surface height amplitude; and ϕ is their phase difference, as above. We integrated this equation over the entire breadth using interpolated values for current amplitude and phase, as above, and a linear interpolation for $b(y)$ between its value at Lewes (59.1 cm, Table 3) and its value at Cape May, New Jersey (70.9 cm, NATIONAL OCEAN SERVICE, 1986). We found

$$\bar{V}_s = (1700 \pm 300)\ \mathrm{m^3\ s^{-1}}$$

with the bulk of the uncertainty arising from phase uncertainty. As LONGUET-HIGGINS (1969) discussed, the Stokes transport represents nonlinearly induced material transport by the wave action (here the M_2 tidal wave) alone. The positive value implies landward transport. The time-averaged Eulerian transport at the mouth must cancel this Stokes transport and include the seaward flow of the mean freshwater volume flux. The latter is about 650 $\mathrm{m^3\ s^{-1}}$ (KETCHUM, 1953). Thus, the Eulerian mean transport at the mouth of Delaware Bay should be about 2350 $\mathrm{m^3\ s^{-1}}$ seaward.

The M_2 tidal currents well seaward of the Bay mouth on the shelf have strongly different features. The map of principal axes of the deepest current meter record from each mooring (Fig. 4) shows that the major axis amplitudes diminish offshore to less than 15 cm $\mathrm{s^{-1}}$ while the minor axes increase. The major axes are aligned roughly normal to the isobaths. BATTISTI and CLARKE (1982) explain these results with their barotropic tidal model for a location 40 km off the New Jersey coast in water of 24 m depth. They predict 13.2 cm $\mathrm{s^{-1}}$ amplitude on the major axis oriented across the local isobath (150°). The ellipticity (ε = 0.54), the clockwise rotation of the current hodograph, and the current phase (90°) all agree well with those we observe 50–70 km from the coast (see moorings 30 and 31). The current phase of 90° implies an alongshore current to the north-northeast at the time of coastal highwater. However, their model neglects the effect of local estuaries, such as Delaware Bay.

As Fig. 4 shows, the region of transition between M_2 tidal currents typical of the Bay mouth and those typical of the local shelf but unaffected by the estuary extends seaward from the mouth roughly 50 km. The transition region is shorter toward the east and longer toward the south off the Delaware coast. On the inner shelf the locus of greatest tidal amplitude intensification above the background shelf levels lies on a line that follows the deep channel south-southeast from Delaware Bay. Evidently this is the preferred pathway on the shelf for the M_2 volume flux passing to and from Delaware Bay. While the shape of this inner shelf transition region is not surprising, its large extent, roughly 50 km, is.

The same pattern for the transition also appears in the phase contour plot shown in Fig. 5. Recall that across the Bay mouth (Fig. 3) the phase was mostly from 60 to 80°. In Fig. 5 the same values lie between the Delaware coast and a line running southeast from the Bay mouth. To the northeast off the New Jersey coast the phase increases to 120°, i.e. maximum currents there occur roughly 2 h earlier than they do at the Bay mouth.

In Fig. 6 we combine the amplitude, major axis orientation, ellipticity and phase properties in Table 3 to create a temporal sequence of vectors at each mooring. We show four such maps: at the time of high water at the coast or tidal phase $\Phi = 0$; at 1/8 the M_2 period later or $\Phi = 45°$; at $\Phi = 90°$; and at $\Phi = 135°$. [The fifth in the series (not shown)

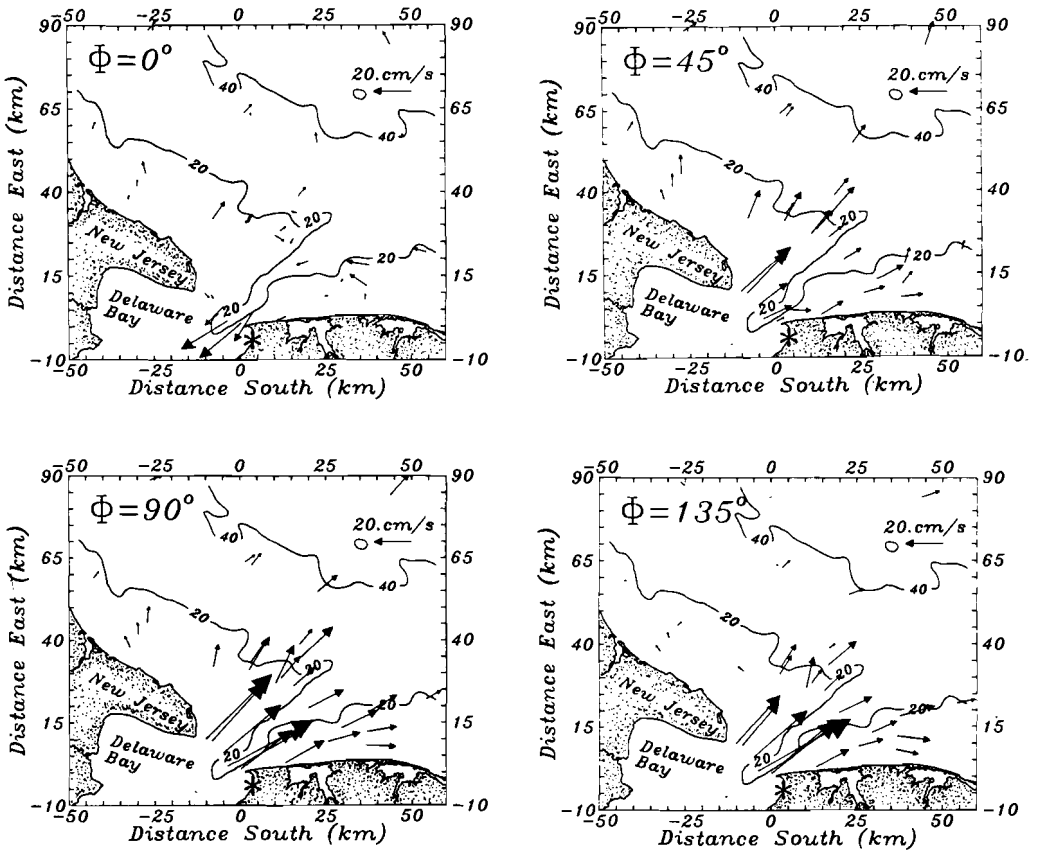

Fig. 6. Maps of M_2 current velocity vectors at four tidal phases: at tidal phase $\Phi = 0°$ (time of high water at the coast), at $\Phi = 45°$ (1/8 tidal period later), at $\Phi = 90°$, and at $\Phi = 135°$. Vectors are shown for each of the sites of Fig. 3. The tail of each vector coincides with the mooring location.

would be at $\Phi = 180°$ and so the currents would be merely the same as the first, but with reversed direction.] At $\Phi = 0$ the flow at the mouth is in the final stages of flood tide while on the shelf currents are weak. At $\Phi = 45°$ the ebb tide has begun at the mouth, while over the shelf a seaward flow diverges from the mouth. The same pattern appears at $\Phi = 90$ and 135°. The ebb currents reach their peak of about 70 cm s^{-1} at the mouth, while over the shelf speeds greater than 20 cm s^{-1} are common in the intensified region that stretches over 50 km to the east and south.

These currents are nearly rectilinear, simply reversing during flood stage (not shown). Off the New Jersey coast to the north, in contrast, the currents remain weak and seem little affected by the outflow from the estuary. Well offshore the currents are rotary and the speeds are low, resembling the model results of BATTISTI and CLARKE (1982).

Intensified M_2 currents on the shelf affect the density and subtidal flow structure because strong flows over bottom topography increase the turbulence intensity. Thus, one might expect a region of locally high vertical mixing. A direct measure of such tidal mixing from bottom turbulence is the parameter SIMPSON and HUNTER (1974) adopted for predicting the occurrence of tidal mixing fronts. Here we compute it as $S = \log_{10}(h/u^3)$

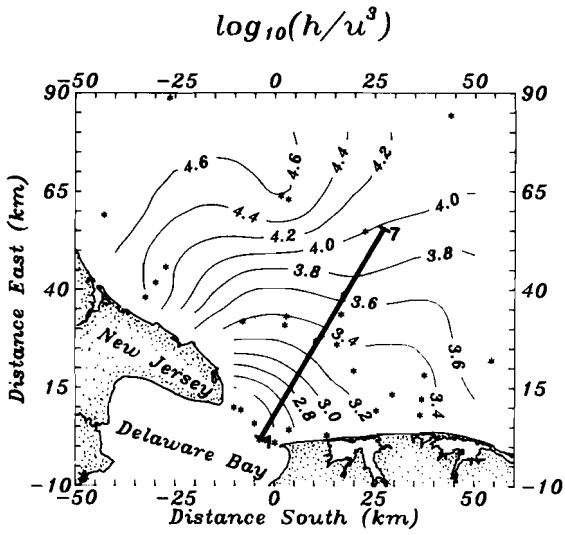

Fig. 7. Contour plot of the parameter $S = \log_{10}(h/u^3)$ for the M_2 current data of Fig. 4. The heavy straight line running seaward from the Bay mouth marks the density transect shown in Fig. 9. Numbers at ends denote corresponding station numbers of the CTD profiles.

where h is the local water depth and u the M_2 major axis current amplitude. We compute S for each of the data points of Fig. 4 and show the results in Fig. 7. The values range from about 2.4 near the Bay mouth to over 4.6 on the New Jersey shelf. The rate of tidal kinetic energy dissipation is proportional to $u^3/h = 10^{-S}$, and thus is over two orders of magnitude greater near the Bay mouth than off New Jersey. The predicted region of intensified tidal mixing stretches from the Bay mouth seaward to the south-southeast. We might select its boundary as the $S = 3.4$ contour in Fig. 7.

During the time of high density stratification in summer we expect tidal mixing on the inner shelf off Delaware Bay to produce a corresponding area of depressed sea surface temperatures as cooler water is mixed upward. We repeatedly observed such a "cold spot" in summertime satellite infrared images of the area and present one in Fig. 8. We contour temperatures in degrees centigrade. Note the correspondence between the area off the Bay mouth enclosed by the 18.5°C isotherm in Fig. 8 and the $S = 3.4$ contour of Fig. 7. The correspondence would be even closer were it not for the advection of warm surface water from Delaware Bay to the south along the Delaware coast by the local density-driven coastal current (GARVINE, 1991). Within the cool feature the temperature drops below 15.5, about 6°C cooler than the surface water well offshore to the southeast.

In Fig. 9 we present yet further evidence of enhanced tidal mixing in this area. For 9 July 1986 we computed the density anomaly σ_t from CTD (conductivity, temperature, depth) profiles at seven stations along the line shown in Fig. 7. The vertical density gradient was small near station 1 (Bay mouth), but increased gradually seaward to station 4. Thereafter, it became large, reflecting the strong mid-shelf pycnocline in summer. The change in stratification along the transect correlates well with the parameter S.

In summary, large amplitude currents are present at the mouth of Delaware Bay, about 70 cm s^{-1}, typical of the estuary. The currents are nearly rectilinear and most of the tidal volume flux passes along a deep channel near the Delaware coast directed northwest–

southeast. Well seaward on the shelf the tidal currents have small amplitude, less than 15 cm s^{-1}, and are rotary with ellipticities of about -0.5 (clockwise rotation). Large tidal volume fluxes to and from the estuary create a transition region on the inner shelf where the currents are intensified and nearly rectilinear. This region extends seaward from the Bay mouth about 50 km and centers on a line that roughly follows the deep channel exiting the mouth onto the shelf. In this region of the shelf tidal mixing erodes vertical density stratification.

4. LONG PERIOD TIDAL CURRENTS

While the short period tidal currents are energetic and easily measured, the long period and steady state tidal currents impact the transport of materials and biota more dramatically. The latter currents achieve this by generating flows with large horizontal displacements and vigorous horizontal stirring of fluid particles. IANNIELLO (1977) emphasized the circulation properties of the long period currents for estuaries and tidal channels, while ZIMMERMAN (1986) computed horizontal dispersion coefficients which resulted from horizontally two-dimensional flows.

While scalar transports due to wave fluxes are still a considerable theoretical problem (DUNKERTON, 1980; MIDDLETON and LODER, 1989), we here suggest that horizontal displacements imply that a particle advects into a different dynamical regime. RIDDERINKHOF and ZIMMERMAN (1990) find enhanced particle dispersion in a spatially variable tidal flow field from numerical simulations of the Dutch Wadden Sea. The amplitude of the

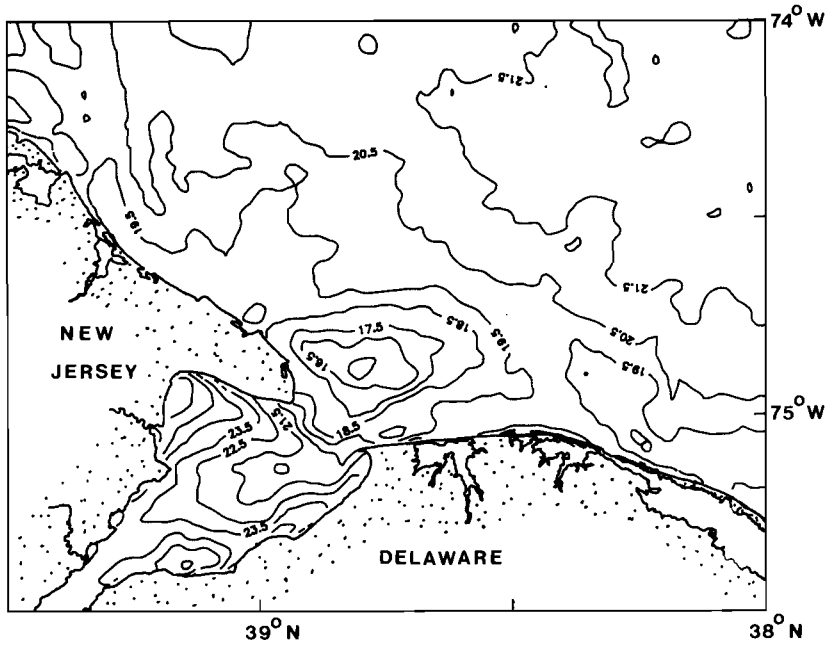

Fig. 8. Sea surface temperature contours (°C) from the NOAA-7 satellite image at 0841 Z on 13 June 1984. Delaware Bay is at the lower left. Note the cool surface temperature off the Bay mouth and over the shelf to the south and east.

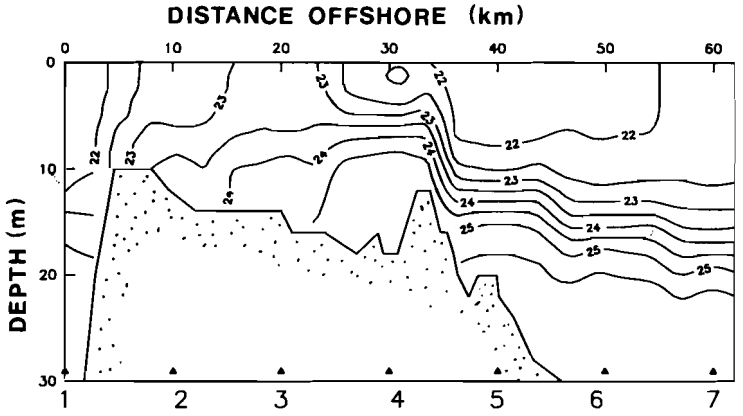

Fig. 9. Vertical section of density anomaly σ_t (kg m^{-3}) along the transect line shown in Fig. 7. Station numbers are given at the bottom. The Bay mouth is at the left (station 1). Data were obtained by CTD profiling on 9 July 1986.

horizontal displacement $\delta = u_o T/\pi$ thus indicates a tidal current constituent's potential impact on transport where u_o and T represent the tidal current's amplitude and period, respectively. For the inner shelf M_2 currents $u_o \cong 25$ cm s^{-1}, and $T \cong 0.5$ days and we thus obtain $\delta \cong 3$ km. But for the lunar monthly constituent M_m we will find in this section $u_0 \cong 3$ cm s^{-1} and $T \cong 28$ days, or $\delta \cong 23$ km. Thus, despite being an order of magnitude weaker in current amplitude, the long period currents have greater displacements because their period is much greater.

Long period tidal currents are either a linear response to astronomical forcing or result from nonlinear dynamics in the short period tidal flow field. For periods up to several months, the primary astronomical forcing constituents are M_f, with $T = 13.66$ days, and M_m, with $T = 27.55$ days. At the latitude of our observations (39°N), however, these forcing constituents are weak, only about 2 and 1%, respectively, of the local M_2 forcing constituent (NEUMANN and PIERSON, 1966). Thus, we expect the astronomically forced long period currents to be about 0.3 cm s^{-1}. We could not detect such weak currents. Consequently, the much more energetic long period currents we report here, typically 3 cm s^{-1}, must have been generated mainly by nonlinearity.

IANNIELLO (1977) derived analytical solutions of currents which weakly nonlinear dynamics generate. For a single short period tidal constituent, e.g. M_2, advection of tidal momentum and other nonlinear effects produce a steady state residual or rectified current as well as the half-period overtide M_4. For two short period constituents, e.g. M_2 and S_2, the same nonlinearities cause, in addition, a current at the difference of the two driving frequencies, or here the M_{sf} current of $T = 14.75$ days. M_2 and N_2, correspondingly, produce the nonlinear contribution to M_m with $T = 27.55$ days.

To provide a visual sense of the importance of these currents we present in Fig. 10 the time series of the 8 day low-pass filtered current from a continuous record where their presence was especially clear. The record is from the first of four from mooring 10 (see Fig. 1 for location) at the mouth of Delaware Bay at 20 m depth and of about 4 months' duration. The component we show is along the local channel direction and is positive into the Bay (landward). The mean landward current of 10.2 cm s^{-1} at this depth arises from the estuarine gravitational circulation. Notice the highly rhythmic current oscillations

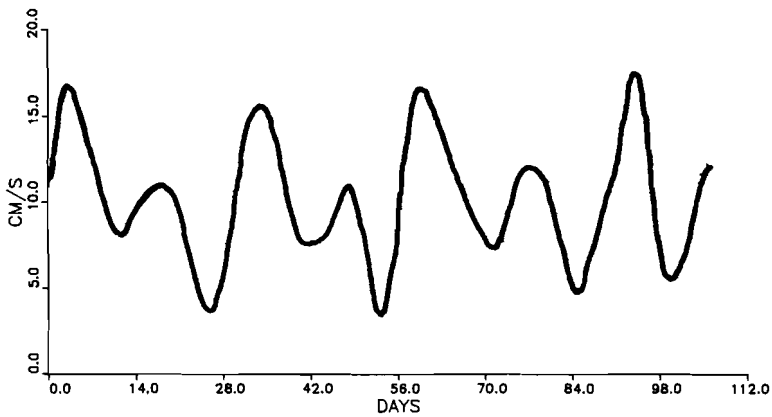

Fig. 10. Eight day low-pass filtered time series of the along-channel velocity component from mooring 10 located at the mouth of Delaware Bay. Note the apparent oscillations at monthly and fortnightly periods superimposed on a 10 cm s^{-1} mean landward flow.

about the mean with apparent periods of about 2 and 4 weeks. Harmonic analysis of the year long record at this location yields M_m and M_{sf} major axis amplitudes of 3.1 and 1.7 cm s^{-1}, respectively. These, in turn, are 4.7 and 2.6% of the local M_2 current amplitude (Table 3).

SIGNELL (1987) simulated the residual flow in Buzzards Bay, Massachusetts with a numerical model of the depth-averaged tidal dynamics. The spatial scales for the residual circulation were of the order 5 km and reflected the local bathymetry. This sensitivity to spatial variability imposes a strong constraint on current meter mooring operations. In order to obtain reliable estimates of M_{sf} and M_m currents, we require long records. Hence we had to service our current meters repeatedly during the data collection period. Generally servicing demands release of the mooring with subsequent resetting.

The new mooring site will then always differ from its predecessor to some extent. Whenever the new site differs enough from the old on the scale of bathymetric variations, the long period currents will differ also. We are aware of two cases in our current records where such significant changes occurred, one of four records at mooring 10 and one of three at mooring 12. Consequently, we excluded these two records from our harmonic analyses. The most serious of the two changes occurred at mooring 10 where before resetting the mooring the ship drifted about 1 km from the intended site. The local isobath at the new site was oriented almost 80° to that at the original site. The M_{sf} and M_m major axes changed by about 55°. Corresponding, but smaller, such variations are thus likely to be present in the analyses we give.

The long period tidal currents represent only one physical process among others causing subtidal variability. Alongshore wind stress (NOBLE *et al.*, 1983) and fresh water discharge that subsequently develops a buoyant outflow (GARVINE, 1991) drive inner shelf currents in our study area. These current responses are broad-banded in frequency. In sharp contrast, the long period tidal currents have discrete, known frequencies. We took advantage of these properties by applying time domain least squares harmonic analysis to our current time series interpreting other than tidal processes as broad-banded noise.

Our task was thus to detect and estimate a harmonic signal of known frequency within noise. To improve the reliability of our estimates we sought to reduce the noise level in our records associated with alongshore wind and fresh water discharge (hereafter termed wind and discharge) by removing that part of the current which was coherent with these two variables. Therefore, we performed standard coherence analysis prior to the harmonic analysis. In frequency space we subtracted the current partially coherent with discharge and wind from the Fourier transformed original current data. Finally, we transformed the incoherent part of the currents back into the time domain and subjected this time series to our harmonic analysis. Our wind data originated from hourly observations at a coastal station at Atlantic City, New Jersey and at an environmental buoy off Delaware Bay, while our discharge data were from daily mean values for the Delaware River at Trenton, New Jersey, the primary source of fresh water for the Delaware estuary. As a check on how the coherence analysis and the inverse Fourier transform would corrupt the data we compared M_2 and K_1 harmonic estimates before and after the spectral analysis. We found that M_2 current phases changed by less than 5°, while M_2 current amplitudes were always reduced by about 5%. These values are larger than the error estimates we presented in Section 2 for M_2 tidal currents, and we thus underestimated rather than overestimated tidal currents. Changes in K_1 ellipse properties are less than their uncertainty estimates for most records.

In Tables 4 and 5 we formally list the properties for the M_{sf} and M_m currents, respectively, which we found from harmonic analysis. We list only results for those analyses that satisfied *all* the following three criteria: (1) total record length greater than 45 data days; (2) a signal to noise ratio (SNR) of no less than two; and (3) an amplitude error of no greater than 100%. (See Appendix A for the description of our error analysis.) We accepted large amplitude errors because for long period tidal currents even reliable order of magnitude estimates are of value and are reported only rarely. Nevertheless, our criteria were met by only 16 analyses for M_{sf} and 19 for M_m from a total of 53 analyses (as

Table 4. M_{sf} *tidal properties*

Mooring	Water depth (m)	Instrument depth (m)	Major axis angle (°)	Major axis amplitude (cm s^{-1})	ε	Phase (°)	SNR
1	23	21	148	2.2 ± 0.7	0.28	72 ± 46	6
2	18	4	94	1.0 ± 0.9	0.11	128 ± 73	2
		12	109	2.0 ± 1.0	0.12	105 ± 56	4
		17	109	1.4 ± 0.7	0.02	105 ± 57	4
4	8	5	10	1.0 ± 0.6	−0.43	102 ± 64	3
5	9	5	−4	0.6 ± 0.4	0.12	127 ± 66	3
		8	5	0.7 ± 0.3	0.04	135 ± 53	5
6	10	5	146	0.4 ± 0.3	−0.20	226 ± 69	3
7	20	5	73	2.9 ± 2.7	−0.26	12 ± 78	2
		15	51	1.9 ± 1.8	−0.32	−26 ± 78	2
10	44	20	111	1.7 ± 0.9	−0.02	107 ± 58	4
11	14	11	113	0.8 ± 0.7	0.02	237 ± 79	2
12	25	3	95	2.1 ± 2.2	−0.09	113 ± 82	2
16	14	6	82	1.8 ± 1.8	−0.41	174 ± 80	2
		10	83	2.4 ± 2.2	−0.33	168 ± 77	2
20	14	6	71	2.2 ± 2.0	0.04	230 ± 78	2

Table 5. M_m *tidal properties*

Mooring	Water depth (m)	Instrument depth (m)	Major axis angle (°)	Major axis amplitude (cm s^{-1})	ε	Phase (°)	SNR
2	18	4	122	1.5 ± 0.6	−0.13	287 ± 51	5
		12	98	2.2 ± 1.0	0.04	257 ± 55	4
		17	106	1.9 ± 0.8	0.10	286 ± 52	5
3	12	6	18	0.9 ± 0.8	−0.20	247 ± 77	2
4	8	5	0	0.8 ± 0.6	−0.54	269 ± 71	3
5	9	5	82	0.5 ± 0.3	−0.31	273 ± 69	3
		8	46	0.5 ± 0.3	−0.10	249 ± 66	3
7	20	5	68	3.0 ± 2.7	0.01	72 ± 77	2
		15	68	1.9 ± 1.7	−0.25	65 ± 75	2
10	44	20	129	3.1 ± 0.7	0.04	250 ± 39	8
12	25	3	111	2.5 ± 2.1	0.55	270 ± 74	2
13	19	16	69	0.7 ± 0.5	−0.27	71 ± 71	3
14	15	6	114	0.6 ± 0.5	−0.63	95 ± 73	2
19	14	6	60	2.4 ± 2.4	−0.14	79 ± 80	2
24	18	7	48	2.0 ± 1.1	0.01	147 ± 56	4
		10	43	2.1 ± 0.9	0.25	81 ± 52	5
		15	68	2.0 ± 1.3	0.05	141 ± 65	3
25	31	8	74	2.6 ± 2.3	−0.48	279 ± 76	2
		27	55	1.4 ± 0.7	−0.09	153 ± 56	4

for M_2 in Table 3). Criteria 2 and 3 above depended strongly on estimated current amplitude. Weaker currents thus tend to have been excluded, unless the local noise level was unusually low or the record length unusually long. In this sense our results in Tables 4 and 5, as well as in subsequent maps for the current ellipses, tend to be biased toward larger amplitude currents.

Figure 11 shows maps of the M_m and M_{sf} principal axes, analogues to Fig. 4 for M_2. We indicate moorings where records failed our criteria by a filled circle. For some of the moorings more than one instrument record gave results that met our criteria. For those cases the axes for the deepest instrument are plotted as orthogonal lines, while the axes for the next instrument upward have arrow heads added to the major axis. Where three levels at the same mooring met the criteria (mooring 2 for M_m and M_{sf} and mooring 24 for M_m; see Fig. 1 for locations) we omitted the uppermost axes to avoid clutter. As Tables 4 and 5 show, where results are available at more than one level the major axis angles and amplitudes are similar, but not as much as those for M_2 (Table 3).

The large majority of major axis amplitudes for both M_m and M_{sf} lie between and 1 and 3 cm s^{-1}. Except in the deep channel of the Bay mouth, long term total mean currents in the study area are less than 5 cm s^{-1} (GARVINE, 1991). Consequently, our results indicate that at many sites the low frequency tides constitute a significant part of the total circulation. In the Bay mouth strong currents are concentrated within the deep entrance channel near the Delaware coast, while over the shallower region toward New Jersey the currents are weaker and nearly orthogonal to the deep channel. To seaward along the deep channel large amplitudes for both constituents occur at mooring 12 (see Fig. 1 for mooring

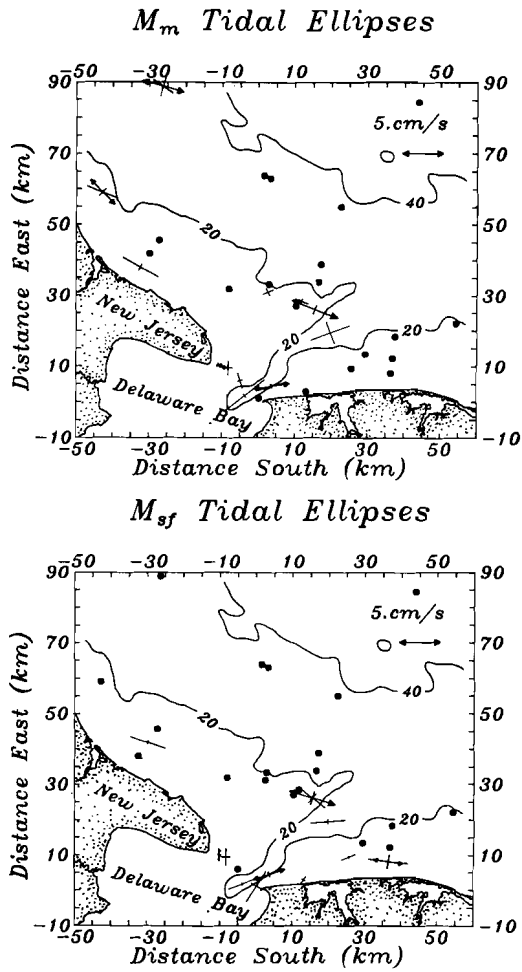

Fig. 11. Tidal current ellipses of M_m (top, 27.56 days) and M_{sf} (bottom, 14.77 days) constituents. Filled circles indicate mooring locations where the data failed our screening criteria. Closed arrow heads indicate that a second instrument above the bottom also provided significant results.

locations) and the major axes are aligned with the channel. Relatively strong currents with major axes directed nearly alongshore occur off the New Jersey and Delaware coasts within 15 km of shore.

5. MEAN TIDAL CURRENTS

The nonlinear processes that cause the M_m and M_{sf} tidal currents also produce mean or steady state tidal currents. These, however, we cannot detect unambiguously because other forcing agents, such as wind stress and fresh water discharge, also contribute to mean currents. Consequently, we resort to theoretical arguments to extract them.

IANNIELLO (1977) presents an argument for connecting the tidal mean current and a low frequency tidal constituent, such as M_m or M_{sf}. His argument assumes that the tidal mean current is driven only by local tidal nonlinearities and that the current is directed primarily along a channel. SIGNELL (1987) later developed a similar argument independently. The substance of the argument is that the low frequency tidal constituents modulate the nonlinear current that results from rectification of the dominant M_2 tide along.

Here we extend Ianniello's argument to flow outside tidal channels for cases where the flow is nearly rectilinear. We write the semi-diurnal surface height at a nearby reference point as

$$\eta = \sum_{i=1}^{3} A_i \cos(\omega_i t + \psi_i) \tag{5}$$

where A_i denotes the amplitude and ψ_i the phase of the three most energetic constituents. Here $i = 1$ denotes the dominant M_2 constituent, $i = 2$ the S_2, and $i = 3$ the N_2 constituent. Then, following IANNIELLO (1977), the nonlinearly induced tidal current at a neighboring point x, y, z is given by

$$q(x,y,z,t) = Q \sum_{i=1}^{3} A_i^2 + 2Q \sum_{k=2}^{3} A_1 A_k \cos[(\omega_1 - \omega_k)t + \psi_1 - \psi_k] + O(QA_2A_3). \tag{6}$$

Here the factor $Q = Q(x,y,z)$ contains all of the spatial variability. The first term on the right has no time dependence and so represents the tidal mean current that we seek. To find it requires that we determine Q. The next two terms given by the summation over k represent modulation of q at the difference frequencies $\omega_1 - \omega_2$ and $\omega_1 - \omega_3$, i.e. the frequencies of M_{sf} and M_m, respectively. Their amplitudes are each proportional to Q, while their phase, $\psi_1 - \psi_k$, is known from the surface height phase in (5). In writing (6) we have neglected in the phase for the two modulation terms the phase shifts $\tan^{-1}[(\omega_1 - \omega_k)/\omega_1]$ because they are small. The last term on the right of (6) gives the order of magnitude of the terms we neglect. Because A_2 and A_3 are typically both small compared to A_1, this term is small also.

In our application we equate the amplitude of each modulation term in (6) to the corresponding major axis amplitude we found by harmonic analysis, provided that the harmonic estimate was reliable, as in Tables 4 and 5. This enables us to find the factor Q and thus to compute the tidal mean current as

$$\bar{q}(x,y,z) = q_{1k} \sum_{i=1}^{3} A_i^2/(2A_1A_k) \tag{7}$$

where q_{1k} is the major axis amplitude for M_{sf} when $k = 2$ and for M_m when $k = 3$. Thus, (7) permits estimation of $\bar{q}$ from either the M_{sf} or the M_m amplitude. Where reliable estimates are available for both, the corresponding values of $\bar{q}$ may be compared to assess the reliability of the method. From (7) we see that when $A_1 > A_k$, i.e. when the M_2 tide is dominant, $\bar{q} > q_{1k}$, or the tidal mean current exceeds the amplitude of both the M_{sf} and M_m constituents. Consequently, the mean current will always exceed the amplitude of a single long period tide. Thus, for example, the effect of the M_{sf} constituent is to strengthen the nonlinearly induced flow during its "spring tide" which is the time of maximum beat

between M_2 and S_2 tides. Crucial in the argument is that the current direction remains unchanged at all times when adding the mean and M_{sf} currents.

Since (6) describes only scalar properties, we apply it only to the flow on the major axis. The direction of the mean flow is then the direction of the long period tide from which it is computed at the time of maximum forcing (maximum beat). This maximum forcing we determine from predicted coastal sea level of the two semi-diurnal tides whose difference frequency gave rise to the oscillatory long period tidal current from which we computed the mean current. For example, M_{sf} currents arise from nonlinear interaction of M_2 and S_2 tidal currents.

We expect this interaction to result in strongest currents at the time of strongest forcing. The time of maximum forcing ("spring tide") is the time when the sea level resulting from the M_2 and S_2 constituents has its maximum. The direction of the mean rectified tidal current is in the direction of the M_{sf} current on its major axis at that time.

Because we infer $\bar{q}$ from our M_{sf} and M_m currents with an untested argument, we established additional criteria for reliability besides those we already used for the low frequency current constituents. Equation (6) predicts the current phase $\Phi = (\psi_1 - \psi_k)$, which we know from the tidal height records at Lewes, Delaware. Meanwhile, our harmonic analyses produced independent estimates for the current phase (Tables 4 and 5). Where the predicted and measured current phase differed by more than 40° we rejected the corresponding result for $\bar{q}$.

Of the possible 35 estimates for $\bar{q}$ (16 from M_{sf}, Table 4, and 19 from M_m, Table 5) we rejected 10. The average of magnitudes of the difference between predicted and observed M_m and M_{sf} current phases [Equations (6) and Tables 4 and 5] is only about 13° for those ellipses which we used to compute the steady state currents. The surviving 25 estimates for tidal mean current we list in Table 6. These give values for current speed and direction at 17 instruments, nine of them in pairs where we have estimates from both constituents. These pairs generally show similar values with the least different pair at mooring 12 and the most different at mooring 5.

We plot $\bar{q}$ in Fig. 12 with the upper map giving $\bar{q}$ derived from M_m and the lower from M_{sf}. As in Fig. 11, filled circles indicate where results failed to meet our criteria. A strong tidal mean seaward flow appears within the deep channel at the Bay mouth and a weak landward flow over the remaining transect between the deep channel and the New Jersey coast. The net flow crossing the Bay mouth section thus appears to be seaward. Such a net tidal outflow is consistent with IANNIELLO's (1977) results for an estuary. Seaward Eulerian mean flow balances the landward Stokes transport (see Section 3) because their sum, the mean Lagrangian transport, must equal only the fresh water discharge. The seaward flow appears to continue well out on the inner shelf to mooring 12 following the deep channel, roughly bounded by the 20 m isobath. Elsewhere on the inner shelf the flow is mainly alongshore to the northeast and surprisingly strong, about 5 cm s^{-1}. This flow thus has a similar speed but the opposite direction of the observed long term total mean flow to the southwest on the Middle Atlantic Bight shelf (BEARDSLEY *et al.*, 1976). The latter mean flow includes tidal as well as wind and density driven flows. Our finding of shelf tidal mean flow to the northeast is consistent with a model study by TEE (1980). He developed a model for the tidal mean flow and applied it to a simple, straight shelf with no alongshelf variations and with semi-diurnal tidal forcing imposed offshore at the shelfbreak. For the northern hemisphere he predicts tidal mean currents of a few centimeters per second directed nearly alongshelf to the right when viewed from offshore.

Table 6. Mean tidal currents

Mooring	Water depth (m)	Instrument depth (m)	Direction (°)	Speed (cm s^{-1})	Constituent used
1	23	21	−32	6.0	M_{sf}
2	18	4	−86	2.7	M_{sf}
			−58	3.4	M_m
		12	−71	5.4	M_{sf}
			−82	5.0	M_m
		17	−71	3.8	M_{sf}
			−84	4.4	M_m
3	12	6	198	2.1	M_m
4	8	5	180	2.7	M_{sf}
			181	1.8	M_m
5	9	5	176	1.6	M_{sf}
			262	1.1	M_m
		8	175	1.9	M_{sf}
			226	1.1	M_m
7	20	5	68	6.9	M_m
		15	68	4.4	M_m
10	44	20	−69	4.6	M_{sf}
			−51	7.1	M_m
12	25	3	−85	5.7	M_{sf}
			−69.	5.7	M_m
13	19	16	69	1.6	M_m
14	15	12	114	1.4	M_m
19	14	6	60	5.5	M_m
24	18	10	43	4.8	M_m
25	31	8	−106	6.0	M_m

Significant tidal mean currents may then be common on continental shelves and near major estuaries. Further observations and model studies to resolve them seem to be timely.

6. SUMMARY

We have described the tidal flow field using records from a large array of current meter moorings deployed between 1983 and 1989 near the mouth of Delaware Bay. We focused on the horizontal distribution of such currents and found large spatial variations for the dominant M_2 flow field. These currents vary in amplitude from about 90 cm s^{-1} at the mouth to only 8 cm s^{-1} 30 km to the north off the coast of New Jersey. Such large horizontal gradients occur in close conjunction with gradients of the bottom topography. Therefore, the mixing capabilities of the tidal currents vary by several orders of magnitude in our study area. We find vertically well mixed waters close to vertically stratified ones during the summer stratified season. Based on the observed M_2 flow field and the associated density field, we identify three distinct dynamical regimes: a far field where the tidal currents are weak and resemble those found elsewhere on the Middle Atlantic Bight shelf well away from estuaries, a near field of locally intensified currents in the vicinity of the deep channel that connects the estuary with the shelf, and finally the mouth of the

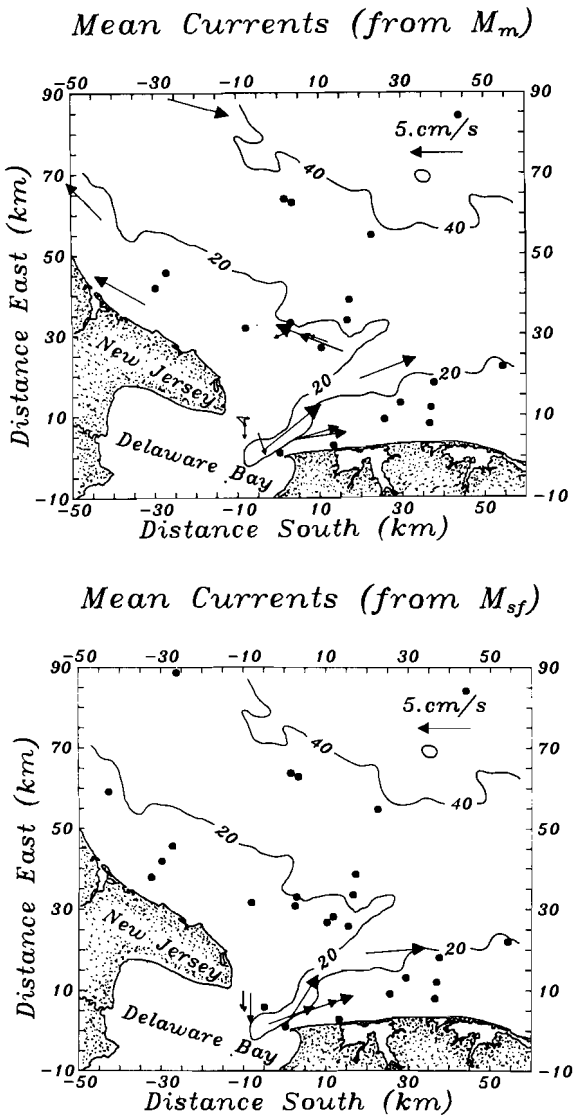

Fig. 12. Tidally rectified mean currents computed from M_m (upper panel) and M_{sf} (lower panel) currents. Note the outflow from Delaware Bay and subsequent turning to the north (to the left viewing offshore).

estuary which is dominated by the interactions between the shelf and the estuary. The tidal volume exchanged between the inner shelf and the Delaware estuary is about 1.5×10^5 m^3 s^{-1}, about two orders of magnitude larger than the Stokes mean volume transport which we estimate as 1.7×10^3 m^3 s^{-1}.

We analysed long period tidal currents through a novel approach which attempts to reduce noise levels in the subtidal frequency band caused by wind or buoyancy forced motion. We thus reliably estimate tidal currents in the same frequency band using time

domain least squares techniques. We developed several screening criteria, all of which depend upon observed signal to noise ratios, in order to establish the reliability of our estimates. We found that monthly and fortnightly currents approaching 3 cm s^{-1} contribute substantially to the subtidal circulation. The flow field at these frequencies is coherent in time and the major axes are closely aligned with the local isobaths. Even off New Jersey where semi-diurnal currents are weakest in our study area, the long-period tidal circulation is strong. Nonlinear generation of currents requires large spatial gradients of properties, not necessarily large currents. We stress again that throughout our study area the spatial variability of semi-diurnal currents is large and thus capable of causing the rectified tidal flow field at low frequencies.

We also computed mean rectified tidal flows from our long period tidal estimates by extending arguments IANNIELLO (1977) gave. The resulting flow field on the inner shelf is surprisingly strong, typically 5 cm s^{-1}, and generally directed opposite to the direction of Kelvin wave phase propagation. These results agree qualitatively with those predicted by TEE (1980).

In summary, we found the transition region between purely estuarine and purely shelf circulations rich in variability. Concentrating on tidal processes only, we discovered three distinctly different dynamical regimes of the M_2 flow field. Long period tidal currents of about 2 cm s^{-1} contribute substantially to the overall subtidal flow as does the tidally rectified mean current of 5 cm s^{-1}. Each of these currents influences the transport and dispersal of matter to and from the estuary profoundly.

Acknowledgements—We are grateful for the help of Kuo-Chuin Wong with data analysis methods and of Claudia Ferdelman for developing computer software. The work was supported by the National Science Foundation through grant OCE-8711299.

APPENDIX A. ERROR ESTIMATION

In order to instill confidence in our estimation of low frequency tidal currents we present here a summary of our methods for estimating the uncertainty of harmonic coefficients we derived. We found three different error estimation algorithms, but none that incorporate directional statistics (MARDIA, 1972). Therefore, we applied scalar statistics to the north and east component of current independently. The most common method to estimate confidence intervals for the amplitude and phase of a sinusoidal fit of observations is to break a time series into pieces, obtain separate harmonic estimates for each piece, average them over all pieces, and use the standard deviation as an error estimate. We rejected this method for two reasons. First, long period tidal constituents would then require excessively long time series. Second, this method fails to treat noise adequately. FILLOUX and SNYDER (1979) proposed an error estimation technique that allows frequency dependent noise to enter the computations of error bounds. Also, their error estimates depend upon the inverse of the coefficient matrix **F** of equation (1). Hence, their technique accounts for error due to the discrete number of frequencies analysed. The main advantage of this method is that the noise does not need to be Gaussian.

The third method has its origin in electrical engineering where detecting known signals in random noise is a common problem. IANNIELLO (1977), following HELSTROM (1960), computed error bounds from known signal to noise ratios (SNR) which we write as

$$\mathrm{SNR} = S_o \left(\frac{T}{N}\right)^{1/2} \tag{A1}$$

where S_o is the amplitude of a sinusoidal signal, T is the record length, and N represents the spectral density of noise at the frequency of the signal. For a known signal to noise ratio variances of the amplitude S_o and phase ϕ are

$$\mathrm{Var}(S_o) = (S_o/\mathrm{SNR})^2 \tag{A2}$$

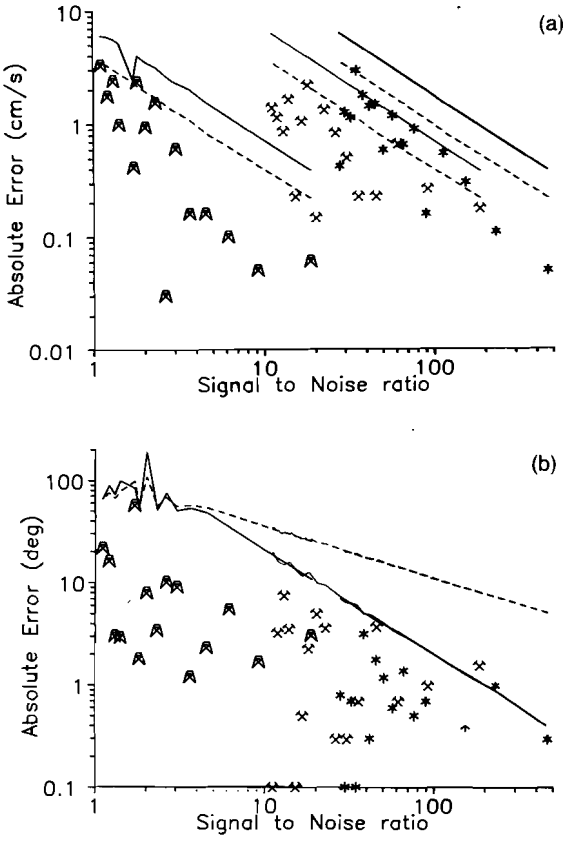

Fig. A1. Comparison of predicted (lines) with actual (symbols) errors in (a) amplitude and (b) phase. Artificial data at three frequencies along with quasi-random noise has been analysed using least squares. The solid lines show the error prediction of FILLOUX and SNYDER (1979) while the dashed ones represent those of HELSTROM (1960) at 95% confidence. The different symbols represent errors at M_2 (stars), S_2 (crossed hammers), and M_{sf} frequencies. Note the large overestimation of errors, especially of phases at low signal to noise ratios.

$$\mathrm{Var}(\phi) = 1/\mathrm{SNR}. \tag{A3}$$

However, one must consider more than just these variance estimates.

There is a probability that a wrong signal is identified instead of the expected signal (false alarm probability) and a probability of detecting the correct signal. Both probabilities depend upon SNR. For example, if we accept a false alarm probability of 10% and a detection probability of 75%, we need SNR > 2 (HELSTROM, 1960). The error estimates (A2) and (A3) must, therefore, be interpreted with respect to the false-alarm and detection probabilities. The major shortcoming of this method is its assumption of white, Gaussian noise. We now compare this method with that of FILLOUX and SNYDER (1979) in a numerical experiment where the error, the noise, and the signal are all known.

In Fig. A1 we summarize our results of 15 harmonic analyses of artifical data which consist of three sinusoids plus noise. We varied the noise but kept the amplitudes at the M_2, S_2, and M_{sf} tidal periods constant at 50, 20, and 2 cm s^{-1} respectively. The symbols represent the true errors of the least squares harmonic analysis which attempts to predict amplitudes and phases of 5 tidal constituents besides M_2, S_2, and M_{sf}. In Fig. A1a the solid and dashed lines shown for each constituent indicate error estimates according to the methods of FILLOUX and SNYDER (1979) and HELSTROM (1960), respectively. The latter error estimates correspond to 95% confidence levels. The slope of

predicted amplitude error estimates as a function of SNR are the same, but FILLOUX and SNYDER (1979) give somewhat higher error. For SNR > 2 the amplitude errors are always less than 3 cm s^{-1}. Figure A1b shows a similar plot for the phase errors. There, both methods perform poorly for SNR < 10, generally overestimating the true phase error by an order of magnitude. The slope of the estimated error as a function of SNR differs now between the two methods: FILLOUX and SNYDER's (1979) error estimate is proportional to $(\mathrm{SNR})^{-2}$ as compared to HELSTROM's (1960) phase error estimate which is proportional to $(\mathrm{SNR})^{-1}$.

For random noise both FILLOUX and SNYDER (1979) and HELSTROM (1960) give upper bounds of phase and amplitude errors. Both methods perform poorly for low SNR, especially for phase error by as much as an order of magnitude. These experiments should be kept in mind when interpreting any error estimation of results from harmonic analyses such as those presented in this study.

We used HELSTROM's (1960) error estimation technique. The noise we obtained from scalar auto-spectral analysis of all east and north components of detided current meter records. We rotated the noise vector onto the direction of the predicted major axis of the tidal ellipse. Using (A2) and (A3) we compute amplitude errors δS_0 and phase errors $\delta\phi$ at the 95% confidence level as

$$\delta S_0 = 1.96(\mathrm{Var}(S_0))^{1/2}$$

$$\delta\phi = 1.96(\mathrm{Var}(\phi))^{1/2}.$$

Often we had many separate but continuous data records for a current meter location. We then computed the noise for the entire record as a weighted average from the individual records.

APPENDIX B. DEFINITION OF PHASE

The harmonic analysis of horizontal current vectors gives amplitudes and phases of the north and east components of tidal constituents. We can also describe the elliptic motion of tidal current vectors as a pair of counter-rotating circles at each frequency (MOOERS, 1973). The sum and differences of the phases and amplitudes of such counter-rotating circles lead to four parameters that define an ellipse. In Tables 2, 3, 4 and 5 we present such ellipse parameters. All parameters except the phase angle we defined in the text.

The phase angle is an angle on the arc of a circle which has the radius of the magnitude of the major axis. The angle is measured positive counter-clockwise (clockwise) for positive (negative) ellipticities.

Figure B1 illustrates how to find the current vector for a given phase angle Φ and a positive ellipticity. There the phase angle is the angle between lines $\overline{OA}$ and $\overline{OB}$. A line perpendicular to $\overline{OA}$ through point B intersects the

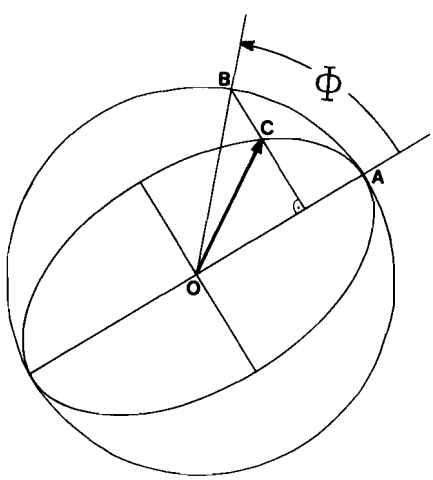

Fig. B1. Definition sketch of tidal phase Φ (positive ellipticity) and the associated current vector on the current ellipse.

ellipse at point C. The vector along $\overline{OC}$ then gives the current at reference time zero or any integer multiple of the constituent period. We define this time as the first predicted M_2 highwater in 1984 at Lewes, Delaware.

REFERENCES

AUBREY D. G. and P. E. SPEER (1985) A study of non-linear tidal propagation in shallow inlet/estuarine systems. Part I: Observations. *Estuarine Coastal and Shelf Science*, **21**, 185–205.

BATTISTI D. S. and A. J. CLARKE (1982) A simple method for estimating barotropic tidal currents on continental margins with specific application to the M_2 tide off the Atlantic and Pacific coasts of the United States. *Journal of Physical Oceanography*, **12**, 8–16.

BEARDSLEY R. C., W. C. BIOCOURT and D. V. HANSEN (1976) Physical oceanography of the Middle Atlantic Bight. *American Society of Limnology and Oceanography*, Special Symposium, **2**, 20–34.

BOWDEN K. F. (1983) *Physical oceanography of coastal waters*, John Wiley, New York.

BUTMAN B., M. NOBLE, D. C. CHAPMAN and R. C. BEARDSLEY (1983) An upper bound for the tidally rectified current at one location on the southern flank of Georges Bank. *Journal of Physical Oceanography*, **13**, 1452–1460.

DRONKERS J. J. (1964) *Tidal computations in rivers and coastal waters*, North Holland, Amsterdam.

DUNKERTON T. (1980) A Lagrangian mean theory of wave, mean-flow interaction with applications to nonacceleration and its breakdown. *Review of Geophysical Space Research*, **18**, 387–400.

FILLOUX J. H. and R. L. SNYDER (1979) A study of tides, set-up, and bottom friction in a shallow semi-enclosed basin. Part I: Field experiment and harmonic analysis. *Journal of Physical Oceanography*, **9**, 158–269.

GARVINE R. W. (1991) Subtidal frequency estuary-shelf interaction: Observations near Delaware Bay. *Journal of Geophysical Research*, **96**, 7049–7064.

HELSTROM C. W. (1960) *Statistical theory of signal detection*, Pergamon Press, Oxford.

HOWARTH M. J. and D. T. PUGH (1983) Observations of tides over the continental shelf of North-West Europe. In: *Physical oceanography of coastal waters*, JOHNS, editor, Elsevier, Amsterdam, pp. 135–188.

IANNIELLO J. P. (1977) Tidally induced residual currents in estuaries of constant breadth and depth. *Journal of Marine Research*, **35**, 755–786.

KETCHUM B. H. (1953) *Preliminary evaluation of the coastal water off Delaware Bay for the disposal of industrial wastes*. Ref. 53–31, Woods Hole Oceanographic Institute, Woods Hole, Massachusetts.

LONGUET-HIGGINS M. S. (1969) On the transport of mass by time-varying ocean currents. *Deep-Sea Research*, **16**, 431–447.

MAAS L. R. M. and J. J. M. VAN HAREN (1987) Observations on the vertical structure of tidal and inertial currents in the central North Sea. *Journal of Marine Research*, **45**, 293–318.

MAGNELL B. A., S. L. SPIEGEL, R. I. SCARLET and J. B. ANDREWS (1980) The relationship of tidal and low-frequency currents on the south slope of Georges Bank. *Journal of Physical Oceanography*, **10**, 1200–1212.

MARDIA K. V. (1972) *Statistics of directional data*, Academic Press, New York.

MAYER D. A. (1982) The structure of circulation: MESA physical oceanographic studies in New York Bight, 2. *Journal of Geophysical Research*, **87**, 9579–9588.

MIDDLETON J. F. and J. W. LODER (1989) Skew fluxes in polarized wave fields. *Journal of Physical Oceanography*, **19**, 68–76.

MOODY J. A., B. BUTMAN, R. C. BEARDSLEY, W. W. BROWN, P. DAIFUKU, J. D. IRISH, D. A. MAYER, H. O. MOFJELD, B. PETRI, S. RAMP, P. SMITH and W. R. WRIGHT (1984) *Atlas of tidal elevation and current observation on the northeast American continental shelf and slope*. U. S. Geological Survey, Bulletin 1611, Alexandria.

MOOERS C. N. K. (1973) A technique for the cross-spectrum analysis of pairs of complex-valued time series with emphasis on properties of polarized components and rotational invariants. *Deep-Sea Research*, **20**, 1129–1141.

NATIONAL OCEAN SERVICE (1986) *Delaware River and Bay tidal circulation and water level forecast atlas*. U.S. Department of Commerce, National Oceanic and Atmospheric Administration, 51 pp.

NEUMANN G. and W. J. PIERSON (1986) *Principles of physical oceanography*, Prentice-Hall, Englewood Cliffs.

NOBLE M., B. BUTMAN and E. WILLIAMS (1983) On the longshelf structure and dynamics of subtidal currents on the eastern United States continental shelf. *Journal of Physical Oceanography*, **13**, 2125–2147.

RIDDERINKHOF H. and J. T. F. ZIMMERMAN (1990) Mixing processes in a numerical model of the Western Dutch Wadden Sea. In: *Residual currents and long-term transport*, R. CHENG, editor, Springer-Verlag, New York, pp. 194–209.